Quasi-One-Dimensional Modeling of Internal Ballistics and Axial Acoustics in Solid Rocket Motors

V. Kalyana Chakravarthy,* Arvind S. Iyer,† and Debasis Chakraborty‡
Defence Research and Development Laboratory, Hyderabad 500 058, India

An unsteady quasi-one-dimensional flow solver for simulating internal ballistics and axial acoustic fluctuations in solid rocket motors is presented in this paper. Higher-order numerical solutions of quasi-one-dimensional governing equations are prone to numerical oscillations due to the nonconservative form of the governing equations and the nonsmooth axial variations of the cross-sectional area. Adding artificial dissipation to a central scheme is found to be inadequate for suppression of such oscillations, and so a simple low dissipation shock-capturing scheme (named SLAU2) is used instead. The inherent numerical dissipation of this scheme is helpful in the proper capturing of steep-fronted acoustic waves (that develop at the onset of triggered instabilities) without undesirable numerical damping of the acoustic waves. Using the new solver, a procedure for computing characteristic frequencies, corresponding mode shapes, and damping rates is proposed and validated for a motor with a cylindrical grain geometry. The quasi-one-dimensional formulation can accommodate either slip or nonslip boundary conditions for axial velocity at grain boundaries and predict damping rates accordingly. The difference in decay rates obtained with these two boundary conditions is shown to be the flow turning contribution.

Nomenclature

A	=	cross-sectional area, m^2
C_p	=	specific heat at constant pressure, J/kg/K
c	=	speed of sound, m/s
D_2	=	artificial diffusivity, m/s
d_h	=	hydraulic diameter, m
e_t	=	specific total internal energy, J/kg
h_t	=	specific enthalpy, J/kg
K	=	specific kinetic energy, m^2/s^2
L	=	length of the combustion chamber, m
M	=	Mach number
$\dot{m}$	=	mass flow rate, kg/s
P_A	=	perimeter per unit area, 1/m
p	=	pressure, Pa
p'	=	pressure fluctuation, Pa
R	=	port radius, m
r_b	=	burn rate, m/s
T_f	=	flame temperature, K
t	=	time, s
u	=	axial velocity, m/s
u'	=	axial velocity fluctuation, m/s
V_{inj}	=	normal injection velocity at the grain boundaries, m/s
x	=	axial coordinate, m
α	=	damping rate, 1/s
γ	=	ratio of specific heats
ρ	=	gas density, m^3
ρ_s	=	propellant density, m^3
ω	=	frequency, 1/s

*Scientist, Directorate of Computational Dynamics.
†Contract Engineer, Defence Research and Development Laboratory; currently Postdoctoral Fellow, Imperial College, London, England SW7 2AZ, United Kingdom.
‡Director, Directorate of Computational Dynamics.

I. Introduction

FLOWS in most solid rocket motors operating as required are sufficiently one-dimensional that quasi-one-dimensional models yield acceptable ballistic predictions. Although some multidimensional effects like those associated with submerged nozzles, slag accumulation, and vortex shedding do require multidimensional modeling, others like boundary-layer and nozzle erosion losses can be dealt within one-dimensional models with empirical correlations [1]. Based on many experiments with solid rocket motors, Blomshield [2] stated that energetic radial modes were very rare in solid motors, whereas tangential modes may appear when double base propellants are used but were hardly ever seen with metallized propellants. This is not surprising, since combustion chambers in solid rocket motors have large length-to-diameter ratios. One-dimensional codes can therefore be very useful for quick linear stability assessment of solid rocket motor designs.

Most of the early ballistics codes were based on a shooting method [1,3]. It involves adjusting, iteratively, the head end pressure and integrating steady quasi-one-dimensional governing equations spatially so that the nozzle entrance conditions correspond to a choked flow condition for the given throat area. This method is unsuitable for simulating transient processes like ignition and wave propagation, not only because of its use of pseudo-steady-state and short nozzle approximations but also its first-order spatial accuracy. Acoustic dynamics in combustion instability studies were handled using linearized equations for the perturbations over the mean flowfield obtained through this shooting method. An eigen-analysis of the linearized equations led to further simplification of the problem through modal decomposition of the perturbations. Only a few dominant large-scale modes could be tracked using a set of ordinary differential equations instead of solving the partial differential equations for wave motion. The complete eigenanalysis and determination of all eigenmodes were computationally very expensive. The spatial averaging technique using a Green's function for the linear wave equations introduced by Culick [4] provided an efficient way of computing the dominant eigenmodes and has been the mainstay of past stability codes. Such relatively inexpensive linear stability analysis could be very useful in rapid evaluation and ruling out of inherently unstable designs.

Triggered instabilities, which are mostly due to nonlinear mechanisms, [2,5–7], cannot be predicted using a linear stability analysis. Flandro et al. [9] noted that motors predicted to be linearly stable using the solid rocket stability prediction (SSP) code [8] could be pulsed into instability [9]. SSP has been modified over time [10] to include some of the nonlinearities for improved stability predictions.

Determination of a large number of modes and corresponding frequencies to deal with steepening of the compression waves into shocklets was computationally very expensive [4]. Computing perturbations using higher-order finite difference or finite volume methods instead of modal representation is always possible, but one has to contend with the numerical problems that nonsmooth area changes and gas dynamic discontinuities present. If they have to be dealt with, the full solution itself can be computed instead of perturbations over a mean [11,12].

Artificial viscosity approaches [13] used to capture shocks without generating numerical oscillations in solutions of Euler and Navier–Stokes equations can also be used for solving quasi-one-dimensional equations [14,15]. However, they do not work as well due to the nonconservation form of the quasi-one-dimensional equations. Problems are encountered if area changes are not smooth as shown in this study. That is one reason why Baum et al. [12,16], and Levine and Baum [17] used a combination of three different schemes for simulating nonlinear instabilities. The more recent works of Loncaric et al. [18], Montesano et al. [19], Baczynski and Greatrix [20], Greatrix [21], and Montesano et al. [22] are based on a nondeterministic random choice method (RCM) developed primarily for capturing discontinuous numerical oscillation-free solutions of hyperbolic conservation laws.

Riemann solver-based deterministic methods [23–28] extended to higher orders using essentially nonoscillatory (ENO) [24,25,27] or discontinuous Galerkin (DG) [26] schemes have also been developed and reported in open literature. The Riemann solver developed by Pekkan and Ucer [23] was used for steady-state and pulsing simulations but only for cylindrical and end burning grains. The axial area variation was smooth along the axis in the former and zero in the latter. The end burning grain corresponded to an inflow boundary condition for a cylindrical chamber. The ENO schemes of d'Agostino and Andrenucci [24] and Ferretti [27] were shown to handle sharp cross-sectional area changes without creating spurious oscillations. The latter work [27] focused on modeling the vorticity–acoustics interaction within a quasi-one-dimensional framework. Cavallini et al. [28] also focused on this aspect using a monotone upstream-centered scheme for conservation laws (MUSCL) approach instead of an ENO scheme to achieve second-order spatial accuracy. The third-order flux-splitting scheme of Willcox et al. [25] was used to test the quasi-steady assumption (often made while making zero- or one-dimensional ballistics predictions) and to study the effects of erosive burning. Unphysical predictions at locations near abrupt area changes were reported with this approach. Except for the work of Shimada et al. [26], none of the aforementioned studies attempted quantification of the damping mechanisms that affected the axial acoustics. In this study, the quasi-one-dimensional results differed significantly from predictions of linear theory and axisymmetric simulations.

There is little doubt that the Riemman solvers used in the past studies [23–28] could capture shocks crisply, but retaining this feature along with an ability to deal with nonsmooth area variations, although possible (especially with the use of ENO schemes), is yet to be demonstrated. The Riemann solvers' ability to capture shocks comes with numerical dissipation, which is undesirable for the proper resolution of wave dynamics. The numerical dissipation of kinetic energy in various solvers/schemes has been studied extensively, but the numerical dissipation of acoustics has received much less attention. Errors due to numerics including dissipation are generally higher at small scales. The large-scale dynamics predicted by various solvers are expected to be quite similar unless small-scale dynamics affect the large scales. Evidence to the contrary has been presented by Shima and Kitamura [29], who showed that numerical dissipation levels for even large-scale acoustics could vary from one Riemann solver to another.

Documented in this paper are efforts to develop an unsteady quasi-one-dimensional model for ballistic and stability predictions with the following requirements. First, the method should be deterministic (unlike the RCM) and based on a single scheme rather than a combination of different schemes. A MUSCL approach would be preferable compared to an ENO scheme for the sake of simplicity.

Numerical oscillations due to nonsmooth area variations and shocks should be minimal. Numerical damping of acoustics should be negligible in comparison with the physical damping. To this end, two different schemes are tested. The first is the second-order MacCormack scheme with artificial dissipation, and the second is the SLAU2 shock-capturing scheme. For steady-state ballistics predictions, comparisons are made with those from a shooting method. Unsteady capabilities are tested by simulating the collapse of compression waves into shocklets and by predicting damping rates associated with different physical processes in a cylindrical motor with zero combustion response to acoustics.

Obviously, the rotational dynamics associated with vortex shedding in segmented motors and parietal vortex shedding [30] cannot be captured using the quasi-one-dimensional equations alone. But, rotational terms associated with unsteady vorticity fields created by axial pressure oscillations, even in simple geometries (like cylindrical grains) that appear in theoretical analyses [31], call into question the use of the quasi-one-dimensional model predictions of damping rates and, consequently, their use for stability predictions. The flow turning loss seems necessary in the stability theory to explain experimental results [32], but its prediction using quasi-one-dimensional modeling, to the authors' knowledge, has never been verified.

II. Governing Equations

Terms included in the quasi-one-dimensional equations used for modeling solid rocket motors differ from one study to another [18,23–26,33] depending on the focus. The equations used here include only the terms that account for cross-sectional area changes in space and time, as well as mass addition normal to the local grain boundary at each axial location:

$$\frac{\partial(\rho A)}{\partial t} + \frac{\partial[\rho u A]}{\partial x} = r_b P_A(\rho_s - \rho)A \tag{1}$$

$$\frac{\partial(\rho u A)}{\partial t} + \frac{\partial[(\rho u^2 + p)A]}{\partial x} = p\frac{\partial A}{\partial x} + r_b P_A(\underline{\rho_s} - \rho)u A \tag{2}$$

$$\frac{\partial(\rho e_t A)}{\partial t} + \frac{\partial[\rho u h_t A]}{\partial x} = r_b P_A[\rho_s C_p T_f - \rho e_t]A \tag{3}$$

The addition of energy (and momentum when the grain boundary is not perpendicular to the axial flow direction) due to the flame speed of the propellant is neglected in comparison with other terms.

The preceding set corresponds to the most conservative form of the equations and is used in most ENO-based schemes [24,25,27] reported in the literature. The first term on the right-hand side of Eq. (2) makes a full conservation form impossible and poses a problem for higher-order spatial discretization. However, this set is referred to as the conservation form. Other schemes (RCM [18] and DG [26]) are based on an alternate form where the effects of area change are included using source terms to one-dimensional Euler equations. This set is referred to as the nonconservation form.

The underlined term in Eq. (2) implies that the incoming mass at the boundary enters the domain with the local axial velocity. This corresponds to a slip boundary condition. Calculations without it correspond to a no-slip boundary condition.

III. Numerical Methods

A second-order explicit Runge–Kutta scheme is used for temporal integration. A finite volume scheme is used for spatial discretization. The fluxes on the cell faces are computed using either a MacCormack scheme [34] or a SLAU2 shock-capturing scheme [35].

The MacCormack scheme is implemented using the conservation forms of the equations listed previously. The fluxes on a face, in odd-numbered steps, are computed using cell-centered quantities to the left in the predictor step and using cell-centered values to the right in the corrector step. The opposite biasing sequence is followed in the

even-numbered time steps to prevent an overall directional bias. The details and performance of this scheme have been well documented [34]. Artificial dissipation terms are added to overcome the sonic glitch and suppress the numerical oscillations in the vicinity of shocks. Artificial diffusivity D_2 is proportional to both the pressure switch (to make it nonzero only around shocks) and the speed of the fastest wave in the system:

$$D_2 \sim \frac{|p_{i+1} - 2p_i + p_{i-1}|}{p_{i+1} + 2p_i + p_{i-1}}|u + c| \qquad (4)$$

Although the scheme can capture shocks, the solutions exhibit postshock numerical oscillations. Although never reported in the context of quasi-one-dimensional models, they are suppressed using fourth-order hyperdiffusion terms [13]. Artificial viscosity approaches with and without these hyperdiffusion terms are considered here.

The simple low dissipation AUSM scheme (SLAU) developed by Shima and Kitamura [29,36] is considered for the present work as an alternative to the MacCormack scheme. It was designed to keep the numerical damping of kinetic energy minimal within the flux splitting framework, but its numerical damping of acoustics was also shown to be much less than that of the Roe scheme [29], on which many of the Riemann solvers in use are based. SLAU2, which is an improved version of SLAU with a more robust shock prediction ability [35], is considered here.

The terms on the left of the Eqs. (A1–A3) are discretized using a finite volume version of the SLAU2 scheme, whereas those on the right are handled as source terms. In the original SLAU2, ρA and pA take the place of ρ and p.

The properties on left and right sides of the face are denoted using subscripts L and R, respectively. The pressure on the face used for the computed flux is obtained using the following equations:

$$A_{\text{face}} p_{\text{face}} = \frac{A_L p_L + A_R p_R}{2} + \frac{f^+(M_L) - f^-(M_R)}{2}(A_L p_L - A_R p_R)$$
$$+ \frac{A_L \rho_L + A_R \rho_R}{2} c_{1/2}[f^+(M_L) + f^-(M_R) - 1] * \sqrt{K_L + K_R} \qquad (5)$$

where

$$f^\pm(M) = \frac{(M \pm |M|)}{2M}, \qquad \text{if } |M| \geq 1$$
$$= \frac{1}{4}(2 \mp M)(M \pm 1)^2, \quad \text{otherwise} \qquad (6)$$

M represents the Mach number computed using the velocity normal to the face and the interfacial speed of sound $c_{1/2}$, and K represents the specific kinetic energy. Kitamura and Shima [35] noted that the SLAU2 is not very sensitive to the specification of the interfacial speed of sound, and so the geometric mean of values on either side is used for simplicity.

The mass flux across the face is computed using following equations:

$$\hat{M} = \min\left[1, \frac{1}{c_{1/2}}\sqrt{K_L + K_R}\right] \qquad (7)$$

$$\chi = (1 - \hat{M})^2 \qquad (8)$$

$$g = \max(\min(M_L, 0), -1)\min(\max(M_R, 0), 1) \qquad (9)$$

$$|V_n|^+ = (1 - g)|V_n| + g|c_{1/2}M_L| \qquad (10)$$

$$|V_n|^- = (1 - g)|V_n| + g|c_{1/2}M_R| \qquad (11)$$

$$V_n = c_{1/2}\frac{\rho_L|M_L| + \rho_R|M_R|}{\rho_L + \rho_R} \qquad (12)$$

$$\dot{m} = \frac{1}{2}[\rho_L A_L(M_L c_{1/2} + |V_n|^+) + \rho_R A_R(M_R c_{1/2} - |V_n|^-)]$$
$$- \frac{\chi}{2}\frac{\Delta(pA)}{c_{1/2}} \qquad (13)$$

$\Delta(pA)$ represents the jump in product of pressure and the cross-sectional area across the cell face. The velocity vector and total specific enthalpy from the upstream side along with the mass flux (as determined by $\dot{m}$) from the preceding equation are used to compute the convective fluxes.

In the first-order version, the left and right values for a given face correspond to the cell-centered values on either side of it. For achieving second-order accuracy in space, the left and right values are calculated using higher-order interpolations from cell centers using the MUSCL approach.

Since both the MacCormack and SLAU2 schemes based on the conservation form of the equations fail to meet the necessary requirements (as demonstrated in later sections), the SLAU2 scheme based on nonconservation forms of the governing equations [18] also had to be considered. In these equations, the left side is exactly the same as in the one-dimensional Euler equations. The terms of the left side are discretized using a finite volume SLAU2 scheme presented in the literature [29,35,36]; whereas those on the right, including the effects of area change, are treated as source terms.

The governing equations and the SLAU2 scheme to solve them are listed in the Appendix.

IV. Results

The simulations reported in this study are for stationary grain geometries, but the unsteady dynamics of all flow quantities are completely time accurate. The area change with time in solid rocket motors is generally very slow, which is why the quasi-steady-state assumption made in many ballistics codes turns out to be reasonable.

Table 1 lists the default values of the parameters used for the simulations. These values are typical for small rocket motors with ammonium perchlorate/hydroxyl-terminated-polybutadiene-based composite propellants. Unless stated otherwise, these are used in all the simulations. Since the combustion response is not simulated, the burn rate is held constant. The default spatial resolution is 5 mm, and the time step is determined by assuming a Courant–Friedrichs–Lewy (CFL) number of 0.4 (limit is 0.5 for stability of a second-order scheme).

Four combustor geometries, shown in Fig. 1, are considered for testing the steady-state performance of the numerical methods. There is no propellant burning on the head end or within the nozzle. The aft-cone and front-cone grain geometries are axisymmetric representations

Table 1   Parameters used for steady-state simulations[a]

Quantity	Value
γ	1.214
ρ_s	1670 kg/m^3
Molecular weight	25.121 kg/mole
Burn rate	6.96 mm/s
Flame temperature	2980 K
Throat diameter	45.2 mm
Length of convergent section of nozzle	12 cm

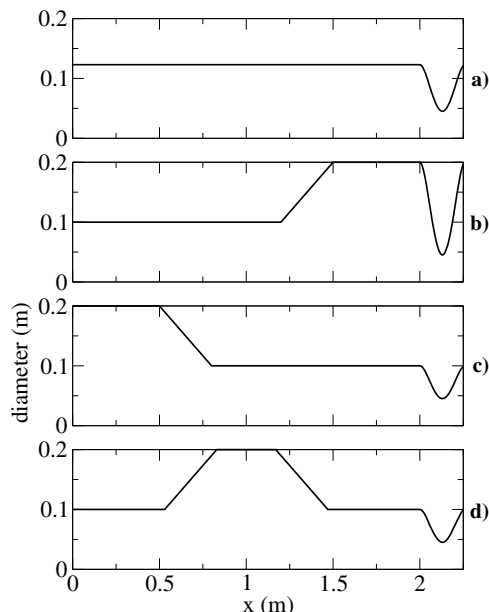[a]Different burn rate of 7.84 mm/s is used for the cylindrical geometry.

Fig. 1   Internal propellant grain geometries used in the simulations. From top to bottom, the geometries are referred to as a) cylindrical, b) aft cone, c) front cone, and d) midcone henceforth.

Fig. 3   Zoomed-in view of pressure profiles for the midcone grain geometry predicted using various schemes. The legend is the same as in Fig. 2.

of finocyl and reverse finocyl grain configurations that are often used to achieve constant thrust in time. All grain geometries except the cylindrical one have the same burning area, and therefore should result in the same chamber pressure (when calculated using a zero-dimensional model). The cone angles used in the study are deliberately chosen to be quite high when compared to values encountered in actual rocket motors, so that the code ability in handling rapid and abrupt cross-sectional area changes can be tested. They are usually kept low to avoid vortex shedding and related problems.

A.   Steady-State Simulations

The midcone grain geometry has all the complexities, like sharp variations in cross-sectional area and discontinuous variations of the source terms (i.e., mass addition stops abruptly when flow enters the nozzle), that can pose problems for numerical modeling. It is used to compare various techniques instead of simulating all the geometries. The solution predicted using a shooting method is used as a reference. The comparisons are made only in the combustion chamber ($0.0\ \text{m} < x < 2.0\ \text{m}$ in Fig. 1) and not in the nozzle ($x > 0.5\ \text{m}$ in Fig. 1) for two reasons. First, the differences between the predictions of various approaches become less evident if the nozzle portion is included due to a steep variation of pressure there. Second, the shooting method does not extend into the nozzle (a short nozzle approximation is used in it).

Figure 2 shows the axial pressure profiles predicted using various schemes. For illustrating the difference in the predictions of various schemes, a zoomed-in view of the predictions around one of the
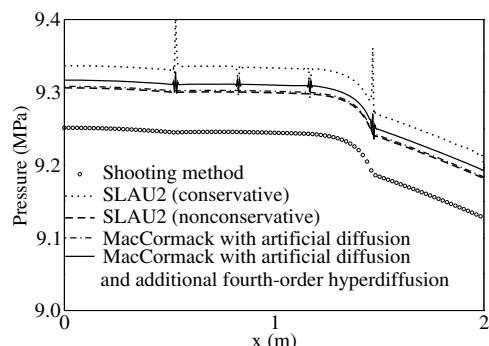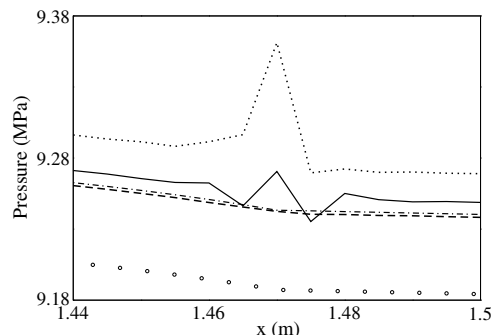
locations where the area changes abruptly is presented in Fig. 3. The MacCormack scheme seems to work really well, even without any artificial viscosity in the subsonic region. The artificial viscosity enables it to handle supersonic flows in the nozzles. Shocks can be captured using artificial viscosity but with undesirable postshock numerical oscillations. Fourth-order dissipation terms are added to suppress postshock oscillations, which arise when only second-order terms are used. However, when these additional fourth-order dissipation terms are added, numerical oscillations are generated at points where area changes are not smooth.

Surprisingly, the SLAU2 scheme based on the conservation form of the equations is quite similar. Instead of oscillations, large spikes are generated near such locations. The SLAU2 scheme based on the nonconservative form of the equations does not have this problem. Overall, the MacCormack scheme with second-order artificial dissipation and the SLAU2 based on the nonconservative form of the equations predict similar results, which also seem acceptable when compared with predictions of the shooting method. Though the profiles are very similar, the predictions are shifted up when compared to the those from the shooting method due to a mass error of about 0.6%. This error is likely a result on the artificial viscosity in the MacCormack, whereas in the case of SLAU2 predictions, it results from use of a nonconservation form of the governing equations. In the rest of this paper, SLAU2 refers to this version of the scheme.

The predictions of the SLAU2 for the front-cone and aft-cone geometries with corresponding predictions of the shooting method are shown in Figs. 4 and 5, respectively. In the latter case, minor oscillations are evident in SLAU2 predictions around the point where the conical section begins. The two-point oscillations have an amplitude that is 0.02% of the mean pressure. These numerical oscillations have the highest possible wave number on a given mesh and are unlikely to affect the large-scale acoustic modes that have the lowest wave numbers.

For further testing, the midcone geometry in which only the cylindrical portion close to the head end ($0.0\ \text{m} < x < 0.5\ \text{m}$ in Fig. 1) has burning propellant is considered. For such a case, the mass addition drops to zero abruptly as the area also changes in a
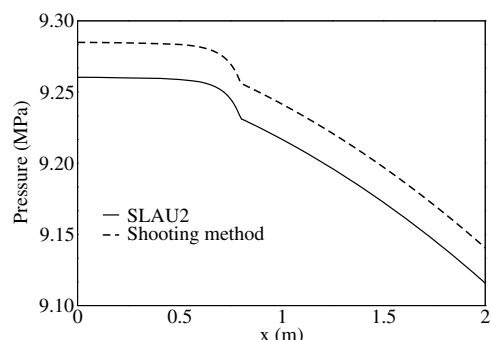

Fig. 2   Comparison of pressure profiles for the midcone grain geometry predicted using various schemes.

Fig. 4   Comparison of pressure profiles predicted for the front-cone grain geometry.
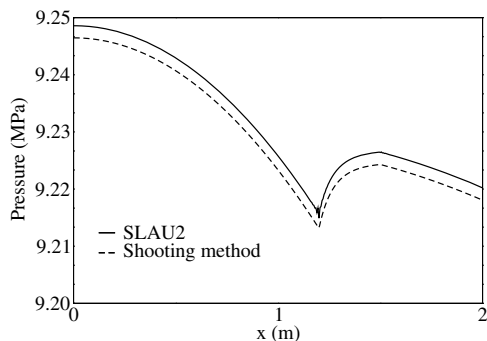
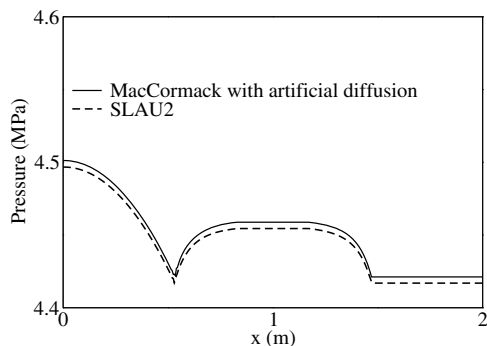**Fig. 5   Comparison of pressure profiles predicted for the aft-cone grain geometry.**

Fig. 6   Comparison of pressure profiles predicted for the midcone grain geometry with burning only in the front cylindrical portion (0.0 m < x < 0.5 m).

nondifferentiable manner. The results predicted for this case using the SLAU2 and MacCormack schemes with second-order artificial dissipation are compared in Fig. 6. In both cases, the numerical oscillations at the corner where burning stops have amplitudes less than 0.02% of the mean pressure.

For the cylindrical grain motor, the quasi-one-dimensional predictions are compared to a reference solution predicted using an axisymmetric simulation performed using FLUENT, a commercial computational fluid dynamics software [37], instead of the ballistics code. The axisymmetric predictions are based on a structured mesh that is uniform in axial the direction and clustered enough near the walls to resolve the laminar boundary layer. As seen in Fig. 7, the overall pressure levels are about 0.3% higher, perhaps due to the additional choking effect of the boundary layer at the throat. The code setup for this axisymmetric case is used for unsteady validation as well.

B.   Unsteady Validation

Two kinds of problems are chosen for unsteady validation. The unsteadiness of the mean flow in the absence of combustion instability can be neglected given that predictions made using many
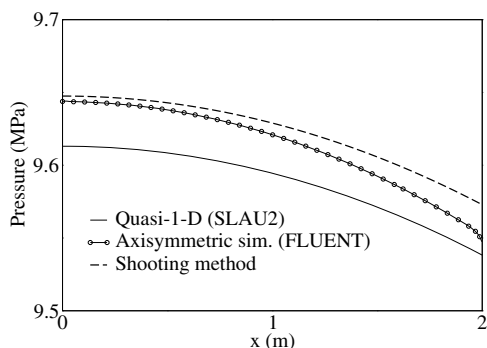

Fig. 7   Comparison of pressure profiles predicted by quasi-1-D and axisymmetric simulations for the cylindrical grain geometry.

ballistics code based on a quasi-steady-state assumption turn out to be quite reasonable after the ignition transients. For combustion instability studies, however, temporal accuracy of the acoustic predictions is very important. The first step in establishing a code's ability to model instabilities is to test its predictions of acoustic damping terms. After doing that, the ability to capture sharp-fronted waves at the onset of triggered instability without numerical oscillations is verified.

1.   Acoustic Damping

All acoustic damping terms for the lower axial modes, except that associated with condensed phase particles, can be computed with reasonable accuracy in a one-dimensional framework provided 1) the numerical damping is negligible and 2) there is no exchange of energy between the axial and transverse modes (i.e., there are no mixed modes).

Shimada et al. [26] investigated the applicability of quasi-one-dimensional approach for modeling axial acoustics and observed that the predicted damping rates differed from those obtained using axisymmetric simulations. Numerical damping was suggested as a possible explanation. Energy transfer to a radial mode was also speculated but reasoned to be unlikely.

Numerical damping notwithstanding, the one-dimensional approach is adequate for capturing losses associated with the nozzle. These losses depend primarily on the nozzle entry Mach number. There is no ambiguity about this quantity in quasi-one-dimensional approaches, whereas in the case of axisymmetric simulations, it is not clear how it should be computed. Whether the average flow velocity is sufficient or some measure of radial nonuniformity is also necessary is unclear. The effect of this nonuniformity might lead to some error that has not been systematically analyzed.

In comparison with the nozzle losses, the flow turning loss has been the subject of much debate. It was captured in Culick's one-dimensional analysis [38] but was missing in the multidimensional formulations [8]. Flandro clarified [39] that it was due to not using the no-slip condition at the grain boundaries. Given that Shimada et al. [26] used an Euler solver that admitted a slip condition rather than a Navier–Stokes solver for multidimensional simulations, the flow turning contribution should have been missing. Yet, the overall loss was higher in multidimensional simulations than in quasi-one-dimensional simulations. The likely explanation is numerical damping or energy transfer to a radial mode, as speculated by them [26].

As pointed out by Flandro [39], the flow can be injected at any specified angle. But, how accurately the losses due to slip and nonslip conditions turn up in quasi-one-dimensional calculations remains unverified. There is reason to expect that some multidimensional effects, like those due to the vorticity field, cannot be captured accurately in a one-dimensional solver [39]. With a slip boundary, the phase of the unsteady fluctuating velocity does not vary with the radial coordinate. This, however, is not the case in the case of viscous calculations. The axial fluctuating pressure gradient is balanced by the unsteady term at the centerline, whereas it is balanced by the unsteady viscous term at the wall. On the grain boundary itself, no slip condition is used for axial velocity, but the axial fluctuating velocity near the wall is not in phase with the same quantity at the centerline:

$$p' \sim \sin(\omega t)\cos(\pi x/L) \qquad (14)$$

$$u'_{\text{centerline}} \sim \cos(\omega t)\sin(\pi x/L) \qquad (15)$$

$$u'_{\text{nearwall}} \sim \sin(\omega t)\sin(\pi x/L) \qquad (16)$$

This phase difference has been confirmed theoretically [31,40], experimentally [41,42], and in the axisymmetric calculations of the present study. The recent analytical solutions of Majdalani [43] indicated that the shear at the wall was in phase with the pressure gradient, as in the preceding equations, but the lag approached $\pi/4$ at higher frequencies. Since the focus here is on lower axial modes, this
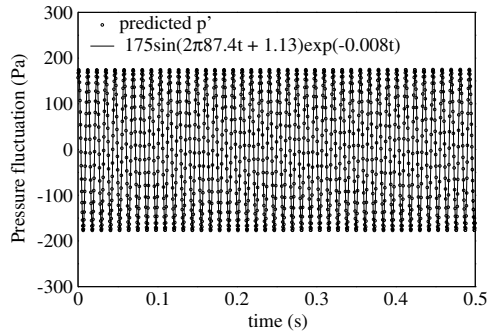
Fig. 8 Simulation of acoustics in closed tube to estimate numerical damping.

phase lag could not be confirmed. The effect of this acoustic velocity phase variation along the radial coordinate is unclear. This part of the study seeks to address numerical damping, energy transfer to radial modes, and boundary condition effects, all of which can affect the accuracy of one-dimensional predictions.

A simple exercise helps in estimating the acoustic damping associated with the numerics. The first harmonic is superimposed on a stagnant state (under standard atmospheric conditions) in a cylindrical chamber on a 2 m length and a 123 mm diameter (similar to the combustion zone in the cylindrical case in Fig. 1), and the temporal evolution is predicted using the Runge–Kutta time-integration scheme and SLAU2 flux splitting spatial discretization scheme over several cycles. The domain is discretized using 400 points, which means that the spatial resolution is the same as that used for rocket motor geometries. The pressure at one of the ends is shown in Fig. 8. Also shown is a decaying sine wave fit to the prediction. The numerical damping rate constant turns out be 0.008/s, which is negligible compared to the characteristic frequency of about 87 Hz. It is also negligible compared to the physical rate constants resulting from the nozzle and flow turning losses in typical rocket motors.

For the cylindrical motor geometry shown in Fig. 1, after a steady state is reached, random velocity fluctuations are added at the head end and pressure data at a few locations are collected over a period of time. This simulates a speaker generating white noise. The frequencies corresponding to eigenmodes stand out in the Fourier transform of the pressure data. If a single point is chosen for calculating the spectrum, an eigenmode that has a node at that location will be missed. So, spectra at multiple points are computed in order to avoid this possibility. The superset of all the peak locations provides the set of eigenfrequencies. Though small deviations can be expected due to the presence of a nozzle instead of a closed end, the acoustics in the cylindrical chamber correspond roughly to pipe harmonics and the nodes can easily be avoided. The spectrum computed using pressure at $x = 0.065$ m (13th grid point from the head end) for the cylindrical geometry is shown Fig. 9. There is a lot of noise in the spectrum generated by random forcing, and so the precise values of the characteristics frequencies are hard to determine. At the lowest characteristic frequency determined from this plot, a sinusoidal forcing is imposed on the head end and pressure data are
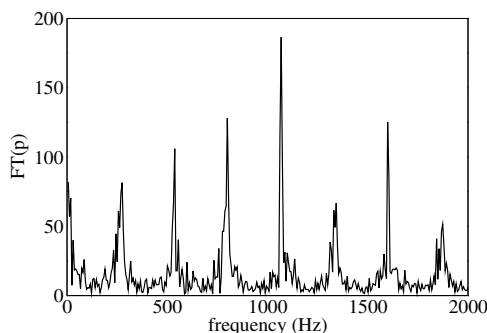
collected. Forcing at this frequency activates only the first mode. The unsteady simulation can be stopped at almost any time. The spatial variation of pressure corresponds to a steady-state profile with an added first mode at some amplitude. With this as an initial condition, the head end forcing is stopped and the pressure is noted as a function of time. The pressure signal is exactly a decaying (monochromatic) sine wave, as expected. If the frequency during decay differs significantly from one used for forcing, the monochrome forcing and decay steps are repeated. If the frequency specification is far from a characteristic frequency or if the initial mode shape was incorrect, there will be multimodal decay of the pressure disturbance, as observed by Javed and Chakraborty [44].

The approach used here helps in two ways. For cylindrical grain geometry, the frequency of the fundamental is computed roughly as $c/2L$, where L is the length of the chamber. It is not clear whether it should include the length of the convergent section of the nozzle. For the geometries simulated, the nozzle is about 12 cm, which is about 6% of the combustion chamber length. So, there is an uncertainty of 6% in estimating the frequency. For the cylindrical grain simulated, the frequency lies between 258 Hz (computed including the convergent section of the nozzle) and 273 Hz (computed by excluding the nozzle portion). Through the exercise detailed previously, the actual frequency for this geometry can be determined exactly.

The same procedure is applied to the axisymmetric code to generate reference values that are used to validate the quasi-one-dimensional predictions. As in the case of steady-state simulations, a no-slip boundary condition is used for axial velocity. The radial velocity at the grain boundary is fixed in space and time to simulate combustion that is nonresponsive to acoustics. Decay rates of the first longitudinal modes in cylindrical motors of four different internal diameters (100, 123, 160, and 200 mm) are computed using the one-dimensional code. For two of these configurations, decay rates are also computed using axisymmetric simulations.

The pressure profiles predicted by one-dimensional (1-D) and axisymmetric codes during decay of the first mode in the motor with a 123 mm diameter are shown in Fig. 10. Decaying sine waves have been fit to extract the decay rates. Frequency predictions differ by about 0.12%, whereas decay rate predictions differ by about 0.67% for this case. Similar comparative plots for the case with a 200 mm diameter are shown in Fig. 11. The differences in frequency and damping rates turn out to be 0.8 and 0.4%, respectively. This verifies that there is no loss of energy to radial modes. This will likely be true as long as the wavelength of a mode is much larger than the radial dimension. For higher modes with shorter wavelengths, there may indeed be a loss to radial modes, depending on the shape of the convergent section of the nozzle.
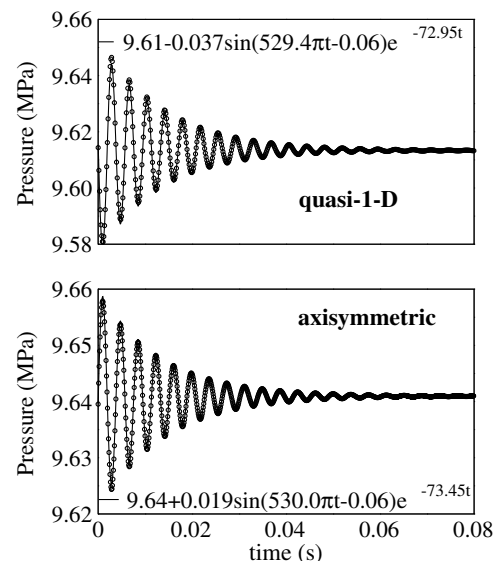

Fig. 10 Decay of first mode pressure pulse for a cylindrical grain geometry with a 0.1234 m diameter.
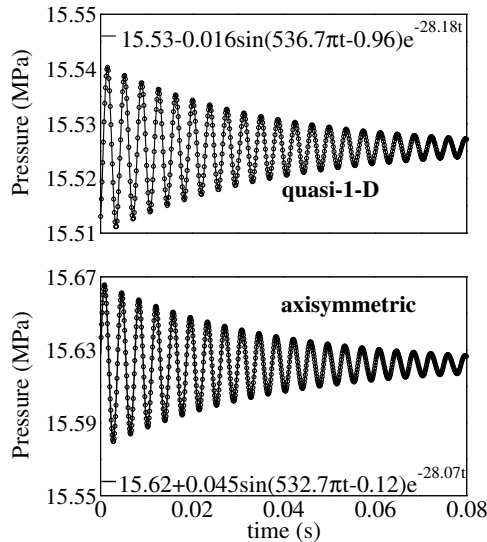

Fig. 9 Frequency spectrum of pressure during random pulsing of a cylindrical motor.

Fig. 11   Decay of first mode pressure pulse for a cylindrical grain geometry with a 0.2 m diameter.

Based on Culick and Yang's linear analysis [45] or the expressions provided by Vuillot and Casalis [46], the decay rate contributions due to the nozzle can be computed analytically for cylindrical geometries. The convective and radiative components are computed as follows:

$$\alpha_{conv} = 2\frac{V_{inj}}{R} \tag{17}$$

$$\alpha_{rad} = (\gamma - 1)\frac{V_{inj}}{R} \tag{18}$$

$$\alpha_{noz} = \alpha_{conv} + \alpha_{rad} = \frac{(\gamma + 1)V_{inj}}{R} \tag{19}$$

The flow turning contribution is estimated to be V_{inj}/R. So, the total decay rate turns out to be $(\gamma + 2)V_{inj}/R$. The predictions made by varying the inner diameter of the cylindrical portion of the combustion chamber while keeping all other parameters the same in the quasi-one-dimensional code are compared with this analytical expression in Fig. 12.

If the one-dimensional code predictions are assumed to be correct (since they compare well with those of a multidimensional code), the analytical expression leads to an underprediction of the decay rate. The percentage error increases as the diameter increases to about 6% at the highest chamber diameter considered here (correspond to length to diameter ratio of 10). As the motor diameter increases (with throat diameter fixed), the nozzle entry Mach number decreases and the linear approximation for the decay rate should be more valid. A better understanding of this discrepancy can be gained if the
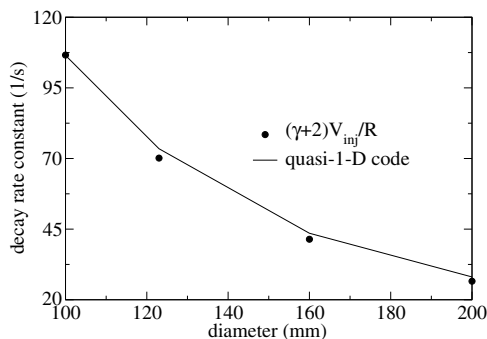

Fig. 12   Variation of total damping with port radius for cylindrical motors.
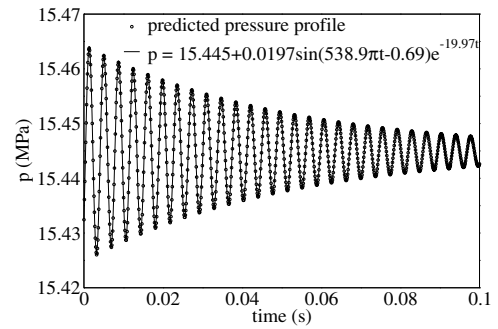

Fig. 13   Decay of first mode pressure pulse with a slip boundary condition in a motor with a cylindrical grain geometry of 0.2 m diameter.

individual contributions can be computed separately using the one-dimensional code.

To separate out the contribution of the flow turning loss from the nozzle damping contribution, the aforementioned exercise was repeated with a slight modification. The momentum and energy equations were modified, assuming that the mass added due to propellant burning had an axial velocity component. In the original equation, the mass addition was in the direction normal to the flow, and so there was no contribution to the momentum equation. The axial component of the mass added could be specified to be either the local instantaneous flow velocity (which corresponded to use of the slip boundary conditions in multidimensional simulations) or the local fluctuation (instantaneous local velocity minus the local time-averaged velocity). Slightly different mean pressure profiles were obtained by using the two different specifications. When the mass added had fluctuations in phase with those of the system, there would be no flow turning loss. For a motor with a 200-mm-diam cylindrical portion, the curve fit to predicted decay of the first mode is shown in Fig. 13; and the decay rate turns out to be 19.97/s. By subtracting this from 28.18/s, obtained in the case with a flow turning loss, a flow turning loss contribution of 8.21/s is estimated for this geometry. This differs from the theoretical value of 8.26/s (V_{inj}/R) by about 0.6%. The flow turning loss is captured by a quasi-one-dimensional code by simply accounting for the no-slip condition, which implies that its magnitude is independent of how rapidly the flow in the chamber turns (i.e., the mean vorticity field near the wall) or on the unsteady vorticity dynamics associated with the acoustic velocity.

Since the flow turning loss is predicted to be very close to its theoretical values (V_{inj}/R), the discrepancy between the predicted and theoretical values of the total decay rate is due to nozzle-related losses. Reducing the length of the convergent portion of the nozzle has a negligible effect on the total decay rate. This, once again, confirms that there is no loss to radial modes in either axisymmetric or quasi-one-dimensional simulations. Equation (18) is based on admittance determined using a short nozzle approximation. Studies have established that this approximation results in an under-prediction. That is the likely reason why the theoretical expression results in lower values of overall damping.

Given that the axisymmetric predictions of various damping contributions are in line with theoretical expressions for cylindrical grain geometries [45], there is no evidence for an additional rotational mechanism associated with the unsteady vorticity field in the acoustic boundary layer that can cancel out the flow turning loss as proposed by Flandro and Majdalani [31].

2.   Nonlinear Effects: Wave Steepening

As the amplitude of pressure disturbance grows, the nonlinear effects become apparent. Linear analysis using superposition of discrete modes is no longer valid. The compression waves steepen, whereas the opposite happens with expansion waves. This leads to creation of sawtoothlike spatial profiles of pressure that have been observed in experiments [9]. Such behavior has been argued to give rise to triggered instabilities and dc shifts [7,9,12].

The ability to capture the sharp-fronted waves is tested by introducing high-frequency (3600 Hz) and high-amplitude sinusoidal
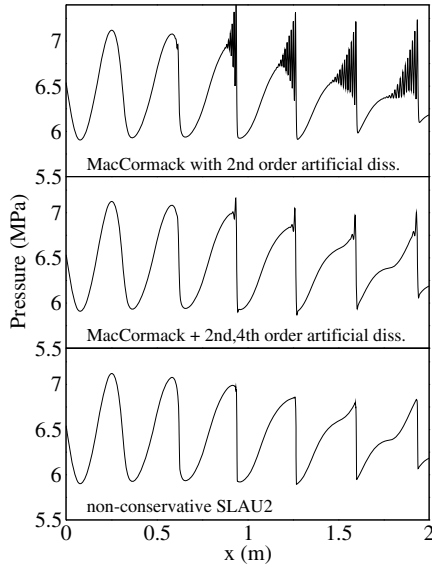
Fig. 14 Simulation of steep front pressure waves using various schemes in the motor with cylindrical geometry.

forcing at the head end of the motor with cylindrical geometry after the steady state has been reached. The high-amplitude compression waves self-steepen to almost shocklike structures. To provide better resolution of these structures, the grid spacing is reduced to 1 mm from 5 mm.

The spatial pressure profiles are plotted in Fig. 14. The conservative MacCormack scheme with second-order artificial dissipation leaves behind unphysical oscillations behind sharp fronts. Baum et al. [16] also observed such oscillations with this scheme. These are not two-point oscillations, and so the harmonic diffusion operator cannot get rid of them. These oscillations are usually controlled by using an additional fourth-order artificial dissipation that mimics a biharmonic operator [13]. This practice works well for steady-state problems with stationary shocks but may not work as well in cases where shocks are moving. Another point to be noted is that it is known to work in one-dimensional and multidimensional simulations; how well it works for quasi-one-dimensional flows (which have nondifferentiable area variations) has never been reported so far. Except for small unphysical kinks immediately behind the shocks, the oscillations are mostly suppressed. Baum et al. [12,16] did not try to control the oscillations generated by the MacCormack scheme. Instead, they moved to a completely different scheme. The same is done here because the fourth-order dissipation leads to problems while dealing with nonsmooth area variations (as seen in Fig. 2). The SLAU2, being a shock-capturing scheme, captures the shocklets crisply without generating numerical oscillations and is considerably simpler than the combination of schemes that et al. constructed [12,16].

V. Conclusions

A quasi-one-dimensional code is developed for simulating flows inside solid rocket motors. The numerical oscillations in its solutions near locations where axial variations of cross-sectional area are nonsmooth are small enough in amplitude to be of no consequence in either ballistic or linear stability predictions. The numerical damping of the acoustic is low enough that the linear damping rates of the eigenmodes can be computed accurately. The shocklike structures that form at the onset of triggered instabilities are captured without any numerical oscillations.

The type of boundary condition for axial velocity at grain boundaries determines the acoustic energy loss due to flow turning. Both slip and nonslip boundary conditions can be simulated in the quasi-one-dimensional framework. By comparing the decay rate predictions made using the two types of boundary conditions, the contribution of the flow turning loss can be estimated accurately. This is despite the fact that the phase of acoustic velocity fluctuations is

known to vary along the radial direction in multidimensional simulations and experiments.

The code is expected to be useful for both ballistic as well as stability predictions. The effects of grain geometry on linear stability are currently being studied and will be reported in the future. Efforts are ongoing to couple it with a grain evolution code to track changes in geometry with time.

Appendix: SLAU2 Scheme for Non-Conservation Forms of Equations

The governing equations for quasi-one-dimensional flow can be recast as one-dimensional Euler equations with the source terms to include the effects of cross-sectional area change in addition to cross-stream mass and heat addition at the walls:

$$\frac{\partial \rho}{\partial t} + \frac{\partial \rho u}{\partial x} = r_b P_A (\rho_s - \rho) - \frac{1}{A}\left[\rho \frac{\partial A}{\partial t} + \rho u \frac{\partial A}{\partial x}\right] \quad (A1)$$

$$\frac{\partial(\rho u)}{\partial t} + \frac{\partial[(\rho u^2 + p)]}{\partial x} = r_b P_A(\rho_s - \rho)uA - \frac{1}{A}\left[\rho u \frac{\partial A}{\partial t} + \rho u^2 \frac{\partial A}{\partial x}\right] \quad (A2)$$

$$\frac{\partial(\rho e_t)}{\partial t} + \frac{\partial[\rho u h_t]}{\partial x} = r_b P_A[\rho_s C_p T_f - \rho e_t] - \frac{1}{A}\left[\rho e_t \frac{\partial A}{\partial t} + \rho u h_t \frac{\partial A}{\partial x}\right] \quad (A3)$$

The terms that account for the area changes can be handled as a source, much like other terms on the right-hand side, whereas the SLAU2 is used to compute the convective and pressure fluxes at the cell faces as follows [35]:

$$p_{\text{face}} = \frac{p_L + p_R}{2} + \frac{f^+(M_L) - f^-(M_R)}{2}(p_L - p_R)$$
$$+ \frac{\rho_L + \rho_R}{2}c_{1/2}[f^+(M_L) + f^-(M_R) - 1] * \sqrt{K_L + K_R} \quad (A4)$$

where

$$f^\pm(M) = \frac{(M \pm |M|)}{2M}, \qquad \text{if } |M| \geq 1$$
$$= \frac{1}{4}(2\mp M)(M \pm 1)^2, \qquad \text{otherwise} \quad (A5)$$

The mass flux across the face is computed using the following equations:

$$\hat{M} = \min\left[1, \frac{1}{c_{1/2}}\sqrt{K_L + K_R}\right] \quad (A6)$$

$$\chi = (1 - \hat{M})^2 \quad (A7)$$

$$g = \max(\min(M_L, 0), -1)\min(\max(M_R, 0), 1) \quad (A8)$$

$$|V_n|^+ = (1 - g)|V_n| + g|c_{1/2}M_L| \quad (A9)$$

$$|V_n|^- = (1 - g)|V_n| + g|c_{1/2}M_R| \quad (A10)$$

$$V_n = c_{1/2}\frac{\rho_L|M_L| + \rho_R|M_R|}{\rho_L + \rho_R} \quad (A11)$$

$$[\rho u]_{\text{face}} = \frac{1}{2}[\rho_L(M_L c_{1/2} + |V_n|^+) + \rho_R(M_R c_{1/2} - |V_n|^-)] - \frac{\chi}{2}\frac{\Delta p}{c_{1/2}}$$

$$(A12)$$

where $[\rho u]_{\text{face}}$ determines the upwinding direction for computing the convective fluxes for mass, momentum, and energy. Inclusion of underlined term in Eq. (A2) corresponds to a slip boundary condition while leaving it out captures the no-slip condition and the flow turning loss.

References

[1] Hermsen, R. W., Lamberty, J. T., and McCormick, R. E., "A Computer Program for the Prediction of Solid Propellant Rocket Motor Performance (SPP)," Air Force Rocket Propulsion Lab. Rept. TR-84-036, Edwards AFB, CA, 1984.

[2] Blomshield, F., "Lessons Learned in Solid Rocket Combustion Instability," AIAA Paper 2007-5803, July 2007.

[3] Hodge, B. K., and Koenig, K., "SOLROC, A Solid Rocket Motor Internal Ballistics Software Element," AIAA Paper 1994-3115, July 1994.

[4] Culick, F. E. C., "Unsteady Motions in Combustion Chambers for Propulsion Systems," NATO-AGARD Rept. AG-AVT-039, 2006.

[5] Hughes, P., and Saber, A., "Nonlinear Combustion Instability in a Solid Propellant Two-Dimensional Window Motor," AIAA Paper 1978-1008, July 1978.

[6] Levine, J. N., and Baum, J. D., "A Numerical Study of Nonlinear Instability Phenomena in Solid Rocketmotors," *AIAA Journal*, Vol. 21, No. 4, 1983, pp. 557–564.
doi:10.2514/3.8113

[7] Malhotra, S., Flandro, G., Malhotra, S., and Flandro, G., "On the Origin of the DC Shift," *Joint Propulsion Conferences*, AIAA Paper 1998-3249, 1997.
doi:10.2514/6.1997-3249

[8] Nickerson, G. R., Culick, F. E. C., and Dang, L. D., "Standard Stability Prediction Program for Solid Rocket Motors," Air Force Rocket Propulsion Lab. Rept. TR-83-017, Edwards AFB, CA, 1983.

[9] Flandro, G. A., Fischbach, S. R., and Majdalani, J., "Nonlinear Rocket Motor Stability Prediction: Limit Amplitude, Triggering, and Mean Pressure Shift," *Physics of Fluids*, Vol. 19, No. 9, 2007, Paper 094101.
doi:10.1063/1.2746042

[10] French, J. C., "Nonlinear Combustion Stability Prediction of SRMs Using SPP/SPP," AIAA Paper 2003-4668, July 2003.

[11] Baum, J. D., Levine, J. N., and Lovine, R. L., "Pulse Triggered Instability in Solid Rocket Motors," *AIAA Journal*, Vol. 22, No. 10, 1984, pp. 1413–1419.
doi:10.2514/3.48581

[12] Baum, J. D., Levine, J. N., and Lovine, R. L., "Pulse Triggered Instability in Rocket Motors: A Comparison Between Predictions and Experiments," *Journal of Propulsion and Power*, Vol. 4, No. 4, 1988, pp. 308–316.
doi:10.2514/3.23068

[13] Jameson, A., Schmidt, W., and Turkel, E., "Numerical Simulation of Euler Equations by Finite Volume Methods Using Runge–Kutta Time Stepping Schemes," AIAA Paper 1981-1250, July 1981.

[14] Coats, D. E., Dang, L., and Nickerson, G. R., "Internal Ballistics Calculations for Nozzleless Solid Rocket Motors," AIAA Paper 1982-1199, July 1982.

[15] Wornom, S. F., and Hafez, M. M., "Calculation of Quasi-One-Dimensional Flows with Shocks," *Computers and Fluids*, Vol. 14, No. 2, 1986, pp. 131–140.
doi:10.1016/0045-7930(86)90005-8

[16] Baum, J. D., Levine, J. N., and Lovine, R. L., "Pulsed Instability in Rocket Motors-A Comparison Between Predictions and Experiments," *Journal of Propulsion and Power*, Vol. 4, No. 4, 1988, pp. 308–316.
doi:10.2514/3.23068

[17] Levine, J. N., and Baum, J. D., "A Numerical Study of Nonlinear Instability Phenomena in Solid Rocket Motors," *AIAA Journal*, Vol. 21, No. 4, 1983, pp. 557–564.
doi:10.2514/3.8113

[18] Loncaric, S., Greatrix, D. R., and Fawaz, Z., "Star-Grain Rocket Motor Nonsteady Internal Ballistics," *Aerospace Science and Technology*, Vol. 8, No. 1, 2004, pp. 47–55.
doi:10.1016/j.ast.2003.09.001

[19] Montesano, J., Behdinan, K., Greatrix, D. R., and Fawaz, Z., "Internal Chamber Modeling of a Solid Rocket Motor: Effects of Coupled Structural and Acoustic Oscillations on Combustion," *Journal of Sound and Vibration*, Vol. 311, Nos. 1–2, 2008, pp. 20–38.
doi:10.1016/j.jsv.2007.08.030

[20] Baczynski, C., and Greatrix, D. R., "Steepness of Grain Geometry Transitions on Instability Symptom Suppression in Solid Rocket Motor," AIAA Paper 2009-5177, July 2009.

[21] Greatrix, D. R., "Parametric Evaluation of Solid Rocket Combustion Instability Behavior," AIAA Paper 2009-5251, July 2009.

[22] Montesano, J., Greatrix, D., Behdinan, K., and Fawaz, Z., "Prediction of Unsteady Non-Linear Combustion Instability in Solid Rocket Motors," *Journal of Aerospace Engineering*, Vol. 223, No. 7, 2009, pp. 901–913.
doi:10.1243/09544100JAERO513

[23] Pekkan, K., and Ucer, A., "One-Dimensional Combustion Instability Studies with Moving Boundaries in an End-Burning Test Motor," AIAA Paper 2002-3608, July 2002.

[24] d'Agostino, L., and Andernucci, M., "Unsteady Ballistic Code for Performance Prediction of Solid Rocket Engines," AIAA Paper 2007-3131, July 2007.

[25] Willcox, M. A., Brewster, M. Q., Tang, K. C., Stewart, D. S., and Kuznetsov, I., "Solid Rocket Motor Internal Ballistics Simulation Using Three-Dimensional Grain Burnback," *Journal of Propulsion and Power*, Vol. 23, No. 3, 2007, pp. 575–584.
doi:10.2514/1.22971

[26] Shimada, T., Hanzawa, M., Morita, T., Yoshikawa, T., and Wada, Y., "Stability Analysis of Solid Rocket Motor Combustion by Computational Fluid Dynamics," *AIAA Journal*, Vol. 46, No. 4, 2008, pp. 947–957.
doi:10.2514/1.31976

[27] Ferretti, V., "Numerical Simulations of Acoustic Resonance of Solid Rocket Motors," Ph.D. Thesis, Univ. of Rome, "La Sapienza," Sapienza, Italy, 2009.

[28] Cavallini, E., Ferretti, V., Favini, B., Di Giacinto, M., and Serraglia, F., "Pressure Oscillations Numerical Simulation in Solid Rocket Motors," AIAA Paper 2012-3445, July 2012.

[29] Shima, E., and Kitamura, K., "On New Simple Low-Dissipation Scheme of AUSM-Family for All Speeds," AIAA Paper 2009-0136, July 2009.

[30] Boyer, G., Casalis, G., and Estivalàĺzes, J. L., "Stability Analysis and Numerical Simulation of Simplified Solid Rocket Motors," *Physics of Fluids*, Vol. 25, No. 8, Aug. 2013, Paper 084109.
doi:10.1063/1.4818552

[31] Flandro, G. A., and Majdalani, J., "Aeroacoustic Instability in Rockets," *AIAA Journal*, Vol. 41, No. 3, 2003, pp. 485–497.
doi:10.2514/2.1971

[32] Blomshield, F., Crump, J., Mathes, H., Stalnaker, R. A., and Beckstead, M., "Stability Testing of Full-Scale Tactical Motors," *Journal of Propulsion and Power*, Vol. 13, No. 3, 1997, pp. 349–355.
doi:10.2514/2.5191

[33] Smith, R., Ellis, M., Xia, G., Sankaran, V., Anderson, W., and Merkle, C. L., "Computational Investigation of Acoustics and Instabilities in a Longitudinal-Mode Rocket Combustor," *AIAA Journal*, Vol. 46, No. 11, 2008, pp. 2659–2673.
doi:10.2514/1.28125

[34] Anderson, J. D., *Computational Fluid Dynamics: The Basics with Applications*, 1st ed., McGraw–Hill, New York, 1995.

[35] Kitamura, K., and Shima, E., "Improvements of Simple Low-Dissipation AUSM Against Shock Instabilities in Consideration of Interfacial Speed of Sound," *European Conference on Computational Fluid Dynamics*, ECCOMAS CFD Paper 1283, Portugal, 2010.

[36] Shima, E., and Kitamura, K., "Parameter-Free Simple Low-Dissipation AUSM-Family Scheme for All Speeds," *AIAA Journal*, Vol. 49, No. 8, 2011, pp. 1693–1709.
doi:10.2514/1.J050905

[37] *ANSYS Fluent User's Guide*, Fluent, Inc., Lebanon, NH, Nov. 2011.

[38] Culick, F. E. C., "The Stability of One-Dimensional Motions in a Rocket Motor," *Combustion Science and Technology*, Vol. 7, No. 4, 1973, pp. 165–175.
doi:10.1080/00102207308952355

[39] Flandro, G. A., "On Flow Turning," AIAA Paper 1995-2730, July 1995.

[40] Majdalani, J., "Boundary-Layer Structure in Cylindrical Rocket Motors," *AIAA Journal*, Vol. 37, No. 4, 1999, pp. 505–508.
doi:10.2514/2.742

[41] Matta, L., and Zinn, B., "Investigation of Flow Turning Loss in a Simulated Unstable Solid Propellant Rocket Motor," AIAA Paper 1993-0115, July 1993.

[42] Brown, R. S., Blackner, A. M., Willoughby, P. G., and Dunlap, R., "Coupling Between Acoustic Velocity Oscillations and Solid Propellant Combustion," *Journal of Propulsion and Power*, Vol. 2, No. 5, 1986, pp. 428–437.
doi:10.2514/3.22925

[43] Majdalani, J., "Exact Navier–Stokes Solution for Pulsatory Viscous Channel Flow with Arbitrary Pressure Gradient," *Journal of Propulsion*

and Power, Vol. 24, No. 6, 2008, pp. 1412–1423.
doi:10.2514/1.37815

[44] Javed, A., and Chakraborty, D., "Damping Coefficient Prediction of Solid Rocket Motor Nozzle Using Computational Fluid Dynamics," *Journal of Propulsion and Power*, Vol. 30, No. 1, 2013, pp. 19–23.
doi:10.2514/1.B35010

[45] Culick, F. E. C., and Yang, V., "Stability Predictions in Rockets," *Nonsteady Burning and Combustion Stabiliiy of Solid Propellants*,

Progress in Astronautics and Aeronautics, AIAA, Washington, D.C., 1992.

[46] Vuillot, F., and Casalis, G., "Motor Flow Instabilities Part 1, Internal Aerodynamics in Solid Rocket Propulsion," NATO Rept. AVT-096, Brussels, Belgium, 2002.

J. C. Oefelein
Associate Editor